ELSEVIER

Journal of Crystal Growth 231 (2001) 95–106

JOURNAL OF CRYSTAL GROWTH

www.elsevier.com/locate/jcrysgro

Floating zone growth of silicon in magnetic fields: IV. Rotating magnetic fields

P. Dold[a,*], A. Cröll[b], M. Lichtensteiger[c], Th. Kaiser[a,1], K.W. Benz[a]

[a] *Kristallographisches Institut der Universität Freiburg, Hebelstrasse 25, D-79104 Freiburg i.Br., Germany*

[b] *Institut für NE-Metalle und Reinststoffe, Technische Universität Freiberg, Leipziger Str. 23, D-09599 Freiberg, Germany*

[c] *USRA, NASA-MSFC, Huntsville, AL 35812, USA*

Received 2 July 2000; accepted 19 May 2001
Communicated by D.T.J. Hurle

Abstract

Transverse rotating magnetic fields ($B_{max} = 7.5\,mT$, $f_{rot} = 50\,Hz$) were applied to the floating zone growth of doped silicon. Non-periodic dopant fluctuations caused by time-dependent thermocapillary convection were considerably reduced by the rotating field. The radial segregation profiles (measured by a spreading resistance probe) became more homogeneous and more symmetric. The transition from a regime dominated by time-dependent thermocapillary convection to a flow state characterized by the rotating magnetic field was determined. This threshold depends on the height of the melt as well as the melt diameter (crystals between 8 and 14 mm have been investigated) and the efficiency of the applied field increases with larger melt zones. For a melt of 14 mm in diameter and an aspect ratio of 1 it is in the range of 2.5–3.75 mT/50 Hz (corresponding to a Taylor number of $Ta = 9.3 \times 10^3$–2.1×10^4). The change from a time-dependent 3D-flow without field to a quasi-axisymmetric 2D-flow with the magnetic field is corroborated by numerical simulations of the flow field: the thermocapillary driven irregular flow rolls are transformed to a nearly axisymmetric flow with high azimuthal flow velocities but reduced axial and radial components.

PACS: 47.20.Dr; 47.62.+q; 47.65.+a; 81.05.Cy; 81.10.Fq

Keywords: A1. Computer simulation; A1. Rotating magnetic fields; A1. Segregation; A1. Thermocapillary convection; A2. Floating zone technique; B2. Semiconducting silicon

1. Introduction

Heat and mass transfer during semiconductor crystal growth are mainly governed by convective flows in the melt. Time-dependent convection in particular leads to segregation on a microscopic scale (dopant striations) as well as a reduced homogeneity of the radial dopant distribution. In

*Corresponding author. Tel.: +49-761-203-6449; fax: +49-761-203-6434.

E-mail address: pit.dold@krist.uni-freiburg.de (P. Dold).

[1] Present address: DaimlerChrysler AG, P.O. Box 710162, D-60491 Frankfurt, Germany.

0022-0248/01/$ - see front matter
PII: S0022-0248(01)01491-9

the absence of radio-frequency heating,[2] buoyancy and thermocapillary (Marangoni) convection are the main sources for melt convection. For small scale (diameter $\leqslant 15$ mm) floating zone silicon crystals, the occurrence of dopant striations is caused by time-dependent thermocapillary convection, which was demonstrated experimentally [1] as well as by numerical simulations [2]. Due to the metallic character of liquid silicon, magnetic fields are the most appropriate tools to influence or control the fluid dynamics during crystal growth processes. Over the last years, the first choice had nearly always been the application of static magnetic fields to suppress time-dependent flows; parts I–III of this article series addresses those possibilities [2–4]. However, severe drawbacks have to be taken into account, particularly in the case of the FZ-growth of silicon: static magnetic fields exert a detrimental effect on the radial dopant distribution due to a coring effect of the remaining flow structure [3]; in addition, thermo-electromagnetic convection (TEMC) was observed in various cases, resulting in enhanced dopant fluctuations instead of reduced ones [4]. Although it was only observed for certain kinds of dopants and concentration levels, it is difficult to predict and to control the appearance of TEMC.

Transverse rotating magnetic fields (RMF), used in steel casting since many years [5,6], follow a different approach: it is not intended to damp the fluid motion, but to dominate the irregular flow structure by overlaying it with fast, azimuthal, axisymmetric flows. Note that the induced azimuthal velocity is much smaller than the rotation frequency of the field itself because of friction and slip. The movement of the melt is driven by the Lorentz force, which is proportional to the square root of the magnetic induction, the rotation frequency, the electrical conductivity of the melt, and the melt radius [7,8]. Furthermore, the strength of the Lorentz force is a function of the melt height and is considerably lower for aspect ratios smaller than approximately 2.5 [9,10]. The driving force of the RMF is usually scaled by the non-dimensional Taylor number (sometimes referred as magnetic Taylor number) as the product of the squared Hartman number Ha and the rotational Reynolds number Re_ω [11]

$$\mathrm{Ha} = BR\sqrt{\frac{\sigma}{\nu\rho}}, \quad \mathrm{Re}_\omega = \frac{\omega_B R^2}{\nu},$$

$$\mathrm{Ta} = \tfrac{1}{2}\,\mathrm{Ha}^2\mathrm{Re}_\omega = \frac{B^2\omega_B R^4\sigma}{2\rho\nu^2},$$

where B is the magnetic induction, ω_B the angular velocity of the field, R the radius, σ the electrical conductivity, ρ the density, and ν the kinematic viscosity.

Up to now, the application of an RMF to crystal growth processes focussed mainly on the improvement of the mass transport during THM growth [12,13], on the control of the oxygen concentration in Czochralski growth [14,15], and the improvement of segregation during Bridgman [16] and floating zone growth [17,18]. RMF-generated flow velocities have been measured for various simplified model arrangements with low melting point liquids (e.g. gallium) [19,20], but in all cases rigid cylinder walls had been used. In the last years, considerable progress has been made with respect to numerical simulations of RMF induced convection. Due to the implementation of the explicit Lorentz force model for finite cylindrical melt volumes [21,22], the flow structure and the transition from laminar convection to Taylor vortex type flow instabilities was demonstrated [9,23].

Recently, the interaction of thermocapillary convection and RMF was investigated numerically by Witkowski and Walker [24]: they distinguished three different regimes, one dominated by Marangoni convection ($\approx \mathrm{Ta} \leqslant 10^4$), an intermediate one for $\mathrm{Ta} = 10^4$–10^5, and a third one ($\approx \mathrm{Ta} \geqslant 10^5$) dominated by the RMF where the thermocapillary flow is reduced considerably.

Compared to our earlier work about the float zone growth of silicon under the influence of magnetic fields [2–4], the aim of the present work is to control the microsegregation and the intensity

[2] Although radio-frequency heating generates, like a RMF, a Lorentz force acting on the fluid due to an induced magnetic field, the situation is completely different due to the small penetration depth of the magnetic field ($\ll 1$ mm) in the case of RF-heating. The resulting flow field is, at least in the area close to the free surface, a highly turbulent one consisting of irregular eddies.

of the dopant inhomogeneities without any drawbacks like coring or thermoelectromagnetic convection.

2. Experimental arrangement

The experiments have been performed in a monoellipsoid mirror furnace similar to the setup described in Ref. [3]. When a radiation frequency heating system cannot be used, the sample size for FZ-Si is severely limited under gravity and the maximum sample diameter is restricted to ≈ 15 mm. To guarantee an oxygen-free atmosphere, the samples are enclosed wall-free in fused quartz ampoules. The feed material consisted of pre-doped sample rods with an average dopant concentrations of 2×10^{18} at/cm^3 (antimony), 1.6×10^{19} at/cm^3 (arsenic), or 6×10^{17} at/cm^3 (phosphorus), respectively. Different sample diameters (8, 10, 12, and 14 mm) have been investigated. The growth velocities were between 1 and 10 mm/min. A total of 25 samples has been grown. No feed or seed rotation was applied to avoid the interaction of striations caused by rotation and those of convective origin. The non-dimensional Marangoni number used to scale the strength of the thermocapillary convection was in the range of approximately 2×10^3–6×10^3, depending on the melt height and the crystal diameter, which influences the heat flow and consequently the characteristic ΔT along the melt surface. The Marangoni number is defined as

$$\mathrm{Ma} = -\frac{\partial\gamma/\partial T \Delta T l}{\rho \nu \chi},$$

where $\partial\gamma/\partial T$ is the temperature dependence of surface tension, ΔT the temperature difference, l the characteristic length (half the zone height), ρ the density, ν the kinematic viscosity, and χ the thermal diffusivity.

The corresponding material parameters for liquid silicon are summarized in Table 1. The growth unit was placed inside a rotating magnetic field device (Fig. 1, left hand side) consisting of six separate coils. Constructing the magnet unit by

Table 1
Material parameters of liquid silicon at the melting point

ρ (g/cm^3) [31]	ν (m^2/s) [32]	χ (m^2/s) [33]	σ (Ω^{-1} m^{-1}) [32]	$\partial\gamma/\partial T$ (N/m K) [34]
2.53	3.5×10^{-7}	1.3×10^{-5}	1.2×10^{6}	-0.28×10^{-3}

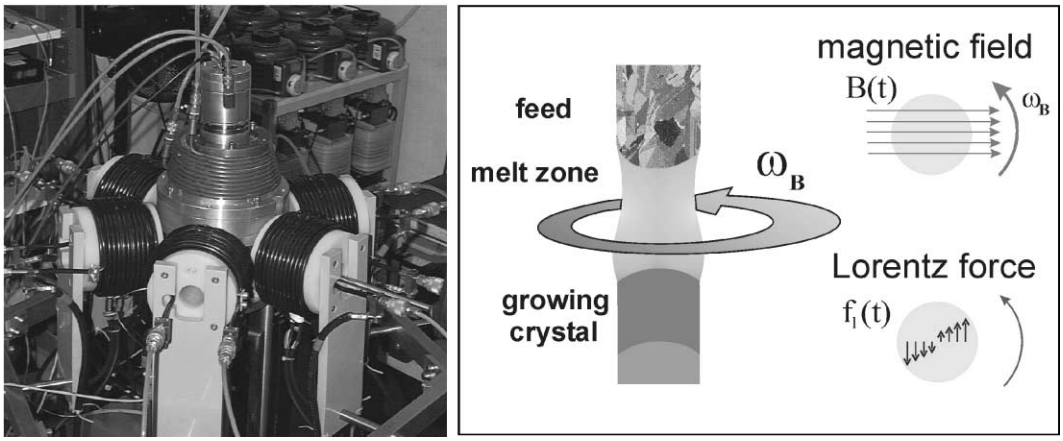

Fig. 1. (a) Experimental setup: a monoellipsoidal mirror furnace is placed in a rotating magnetic field device consisting of three separate Helmholtz-type coil pairs; (b) sketch of the orientation of the magnetic field with respect to the melt zone and direction of the induced Lorentz force.

single coils results in a maximum degree of freedom with respect to the available magnet diameter. The coils are powered with conventional 50 Hz AC, opposite coils are connected to form Helmholtz-type coil pairs. The magnetic induction can be controlled continuously between 0 and 7.5 mT, different induction levels can be adjusted within a few seconds. The geometry of the coils is large in comparison to the melt volume resulting in a homogenous field distribution within the melt zone.

In the case of silicon with a diameter of 14 mm, a maximum Hartmann number of 2 results, the maximum Taylor number is 8.5×10^4. The skin depth calculates to 65 mm (in the case of 50 Hz) and therefore related effects are negligible. The orientation of the field relative to the melt zone is shown in Fig. 1 on the right hand side as well as the direction of the induced Lorentz force.

The grown crystals were cut lengthwise parallel to the {1 1 0}-plane, polished, and etched to reveal compositional non-uniformities. Different characterization methods have been used like Nomarski interference contrast microscopy (NDIC), frequency analysis of the NDIC microscope images, and, for a quantitative assessment of the dopant fluctuations, spreading resistance (SR) measurements. A more detailed description of the characterization methods is given in Ref. [3].

3. Results

3.1. Experimental results: dopant distribution

A magnetic field grown Si : Sb crystal ($\varnothing = 14$ mm) is shown in Fig. 2, "as grown" on the left hand side and a composite NDIC

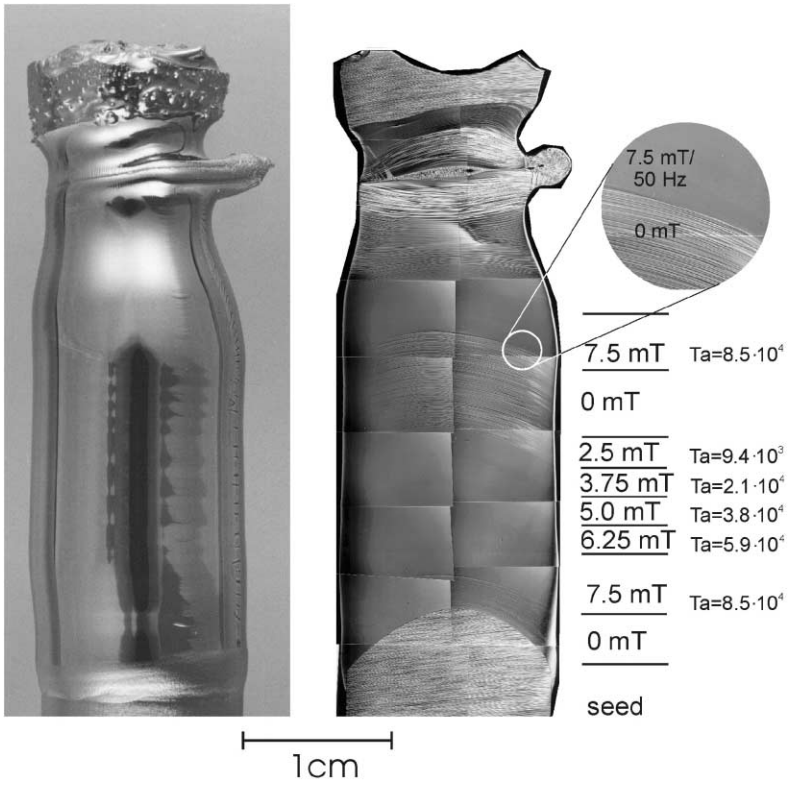

Fig. 2. Si : Sb crystal: "as grown" (left hand side) and a composite NDIC micrograph after cutting, polishing and etching (right hand side). The microsegregation (striation pattern) changes significantly upon application of the RMF.

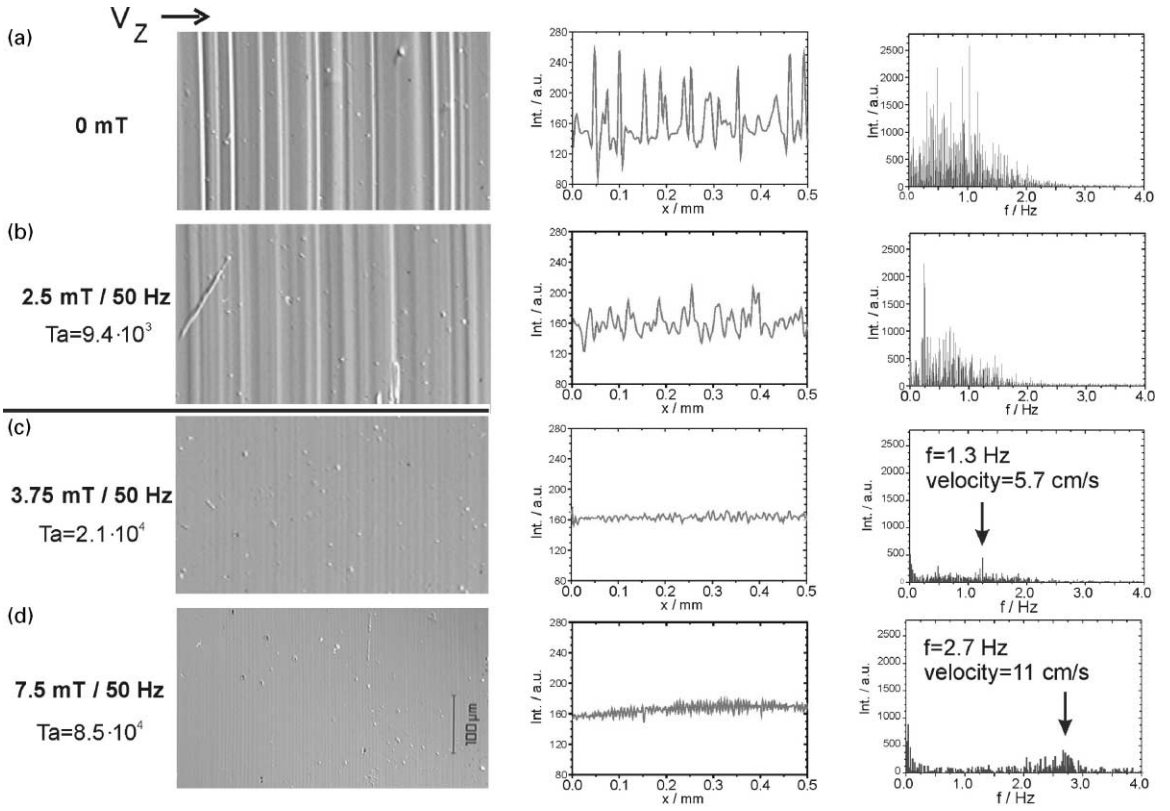

Fig. 3. Striation patterns (left and middle column) and corresponding frequency distribution (right column). The plots of the center column show the intensity of the interference contrast microscopy images given on the left hand side. In the case of 14 mm samples (aspect ratio = 1), the most significant change in the intensity of the dopant non-uniformities was found between 2.5 and 3.75 mT/50 Hz or corresponding Taylor numbers $Ta = 9.2 \times 10^3$ and $Ta = 2.1 \times 10^4$, respectively.

micrograph of the cut, polished, and etched axial section on the right hand side. The magnetic induction was altered several times during the growth run which had no effect on the zone shape or the diameter control of the crystal. The aspect ratio of the floating zone was approximately 1. A strong reduction of the dopant striations is evident in the parts grown with an RMF, as can be seen in the magnified section in Fig. 2 as well as in Fig. 3. Without magnetic field (Fig. 3a), the distribution of the dopant non-uniformities is irregular. The frequency spectra as shown in Fig. 3 were calculated from the brightness signal of a trace taken parallel to the growth direction from the NDIC image and transformed into the time-domain by using the average translation rate of 1 mm/min. They reveal no specific frequencies but a broad distribution approximately between 0.1 and 2 Hz. This corresponds to a thickness of the dopant striae approximately between 8 and 170 μm. The signal intensity and the frequency spectra change only slightly by applying a RMF of 2.5 mT ($Ta = 9.4 \times 10^3$), but a strong transition in the characteristic microstructure of the dopant distribution is found between 2.5 and 3.75 mT ($Ta = 9.4 \times 10^3$–2.1×10^4). A drastic reduction of the intensity of the nonuniformities is observed and the remaining striations show a spacing of approximately 12 μm, corresponding to a characteristic frequency of 1.3 Hz. Increasing the magnetic induction to 7.5 mT ($Ta = 8.5 \times 10^4$), the characteristic frequency shifts to $\approx$2.7 Hz (equivalent to 6 μm). Assuming that these quasi-periodic, high frequency striations result from the flow

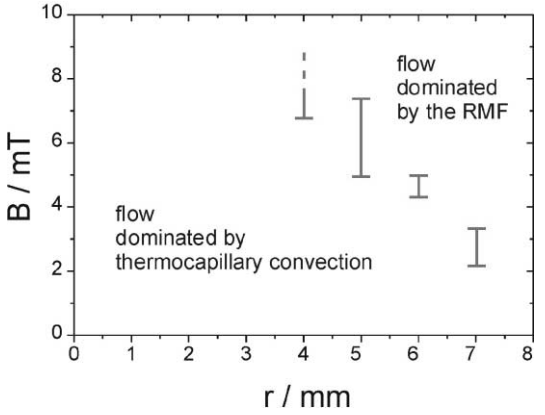

Fig. 4. Threshold values for the transition from a flow regime dominated by thermocapillary convection to a flow governed by RMF as a function of the melt diameter. The transition points were determined for an aspect ratio of 1.

induced by the RMF, i.e. each dopant striation corresponds to one azimuthal revolution of the fluid driven by the rotating Lorentz force, one can easily calculate the maximum azimuthal flow velocity. The maximum velocity is reached at the free surface (because of the slip condition) resulting in a flow velocity of approximately 5.7 cm/s in the case of 3.75 mT and 11 cm/s for 7.5 mT.

As one would expect, the threshold from the thermocapillary—to the RMF-dominated regime shifts to higher magnetic inductions for smaller melt diameters (Fig. 4). In the case of 8 mm, the transition point could not be reached at all with the field strength available. When assessing these results, it has to be considered that the threshold depends not only on the diameter (i.e. the Taylor number) but also on the strength of the Marangoni convection, which will be slightly reduced for larger crystal diameters because of decreased temperature gradients at the solid–liquid interfaces due to a higher axial heat flux. In any case, the efficiency of the RMF increases with larger melt diameters and lower magnetic field strengths are required to dominate the time-dependent natural convection. A similar behaviour was described for the interaction of time-dependent buoyancy convection and RMF [18,19]. There, the transition point from a buoyancy dominated flow (expressed in terms of the non-dimensional Rayleigh-number) to a RMF-dominated regime scales with the square root of the Taylor number like $\mathrm{Ra} \sim \sqrt{\mathrm{Ta}}$.

The reduced fluctuation rate as observed in the NDIC-images is also present in the axial spreading resistance measurements (Fig. 5). In Fig. 5a, the initial part of a Si : As crystal (8 mm $\varnothing$) grown partially without magnetic field and partially with a field of 7.5 mT/50 Hz ($\mathrm{Ta} = 9.0 \times 10^3$) is presented. No significant difference is observed between the curves measured in the center and at the periphery. The point $x = 0$ indicates the initial interface position; due to a flattening of the interface curvature, the peripheral part of the crystal grew faster than the center one and the markers indicating the transition are at different x-positions. In addition to the reduced dopant fluctuations, the slope of the axial segregation curve changes due to the RMF. The alteration is only weak for the case of $\mathrm{Ta} = 9.0 \times 10^3$ but becomes significant for $\mathrm{Ta} = 8.5 \times 10^4$ (Fig. 5b—in this case, the step widths of the SR-probe were larger than the average striae spacings, therefore the change in the microsegregation is not apparent in the SR measurements).

Dominating the time-dependent thermocapillary convection by the azimuthal forced flow results in an improved radial dopant distribution profile (Fig. 6). Two effects have been observed: first, the fluctuations are strongly reduced which agrees with the NDIC results and the axial segregation measurements, and second, the shape of the profile changes. It becomes flatter and more symmetric when the field is applied. The higher concentration level in the case of $B = 7.5$ ($\mathrm{Ta} = 8.5 \times 10^4$) in Fig. 6 is effected by the axial segregation: the final plateau of the dopant concentration was not attained and is actually impossible to obtain at all in a mono-ellipsoid mirror furnace due to the limited processing length.

3.2. Fluid flow: numerical simulations

The commercial software FIDAP [25] was used to solve the coupled system of partial differential equations numerically. The code is based on the finite element method. A detailed description of

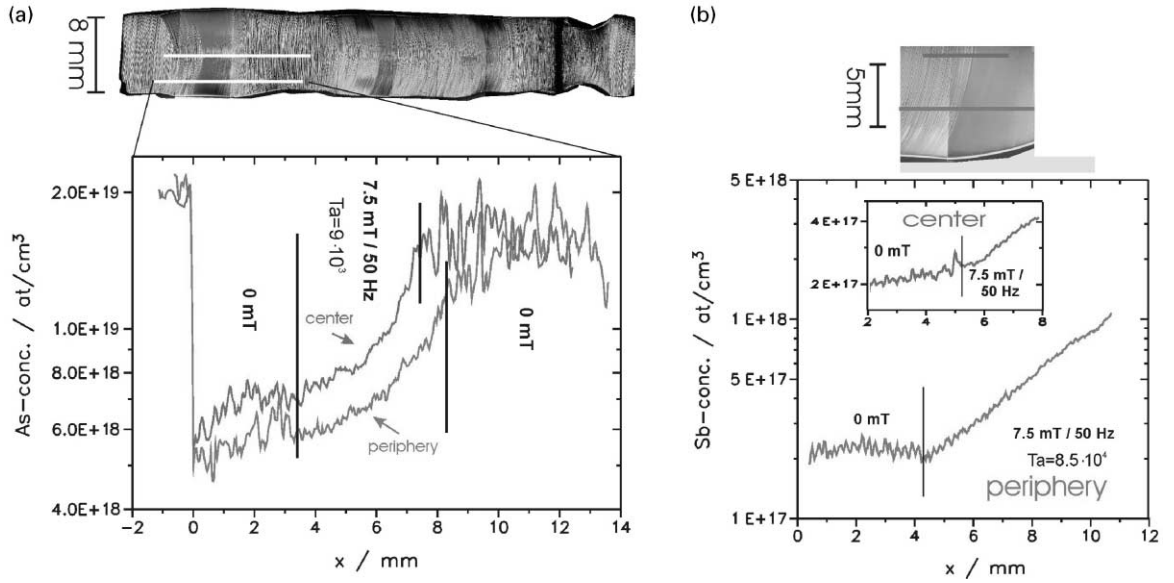

Fig. 5. Axial segregation of an 8 mm Si : As crystal (a) and a 14 mm Si : Sb crystal. (b) Details are explained in the text.

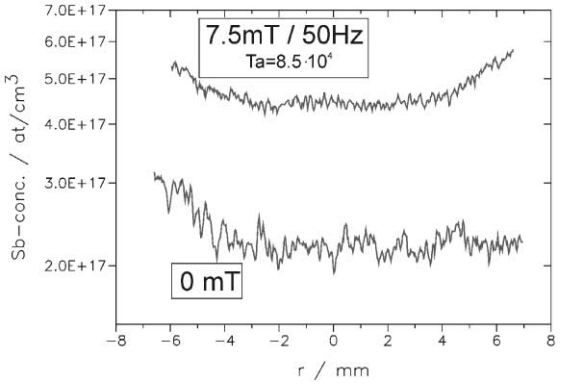

Fig. 6. Radial dopant distribution of an Sb-doped silicon crystal. The fluctuations are reduced due to the RMF and the shape of the profile becomes more axisymmetric.

the equations (Navier–Stokes equations in the Boussinesq approximation together with the continuity equation) describing fluid motion and heat transfer due to thermocapillary convection in a silicon floating zone are given in Ref. [2], together with the non-dimensionalization scheme and the boundary conditions used. The numerical treatment of transverse rotating magnetic fields, the theoretical background, the basic equations (Navier–Stokes equations with the Lorentz force term and the induction equation), the applied approximations (undisturbed magnetic induction and an induced fluid flow velocity much smaller than the rotation of the magnetic field), and the explicit formulation of the Lorentz force distribution in finite cylinders are explained in Ref. [9] and will not be repeated here.

The computational domain of the melt zone is fixed, fluctuations of the free surface or pinching effects due to the RMF are neglected, an assumption which is justified by the experimental observations. The shape of the floating zone was calculated by solving the Young–Laplace equation $\Delta p = \gamma H$ (with γ: surface tension and H: curvature).

In contrast to the simulations presented in Refs. [2,9], the transverse rotating magnetic field is now acting on a free melt surface. In the case of an infinite cylinder, the radial velocity profile can be solved analytically. Due to the translation symmetry along the cylinder axis and the rotation symmetry, the Navier–Stokes equations are

reduced to normal 2nd order partial differential equations and $u_\varphi(r)$ can be solved using a polynomial approach, we obtain

$$u_\varphi^{\text{rigid}}(r) = \frac{\sigma\omega B_0^2 R^3}{16\rho\nu}\left(\frac{r}{R} - \left(\frac{r}{R}\right)^3\right)$$

with boundary conditions (no-slip):

$$u_\varphi\big|_{r=0} = 0, \quad u_\varphi\big|_{r=R} = 0$$

and in the case of a free surface where we assume slip condition [26] in general, a liquid column with free surface would asymptotically approach the rotation frequency of the RMF

$$u_\varphi^{\text{free}}(r) = \frac{3\sigma\omega B_0^2 R^3}{16\rho\nu}\left(\frac{r}{R} - \frac{1}{3}\left(\frac{r}{R}\right)^3\right)$$

with boundary conditions (slip conditions):

$$u_\varphi\bigg|_{r=0} = 0, \quad \frac{\partial u_\varphi}{\partial r}\bigg|_{r=R} = 0.$$

The ratio between the maximum velocities in a cylinder of rigid boundaries compared to a melt with free surfaces calculates to

$$\frac{u_{\varphi\,\max}^{\text{free}}}{u_{\varphi\,\max}^{\text{rigid}}} = 3\sqrt{3}$$

i.e. using the same magnetic field, a velocity more than five times faster is achieved in the case of a free surface. The corresponding velocity profiles are plotted in Fig. 7, the velocities are normalized on the base of the $u_{\varphi\,\max}$ of the rigid cylinder. Contrary to the case of the fixed container walls, where the maximum is located at $r = 1/\sqrt{3}R = 0.58\ R$, the maximum shifts to $r = R$ for the free surface case.

For the numerical simulation of the RMF acting on a free melt zone of finite length, we need the boundary condition for the electrical potential Φ to guarantee that no currents normal to the liquid surface occur, in addition to the boundary conditions formulated in Refs. [2,9]

on the free surface:

$$\nabla\phi\cdot\boldsymbol{n} = (\boldsymbol{n}\times(\boldsymbol{u} - \omega r\boldsymbol{e}_\varphi))\,B_0\boldsymbol{e}_x = \frac{-B_0(u_{t1} - \omega r)\cos(\varphi)r'(z)}{(1 + r'(z)^2)^{1/2}} + B_0 u_{t2}\sin(\varphi)$$

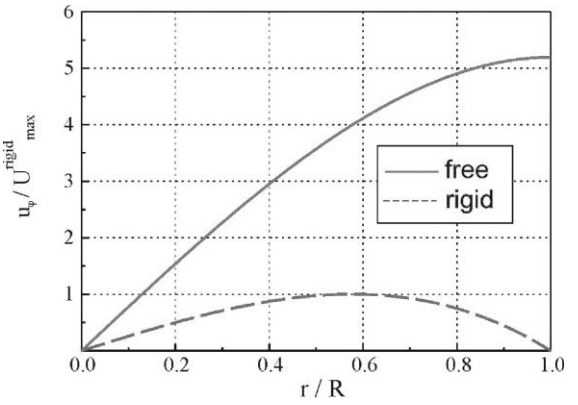

Fig. 7. Normalized radial velocity profiles obtained by analytical calculations for the case of rigid cylinder walls (lower curve) and for a free melt zone. In the case of a free surface, the maximum velocity is more than five times higher and the fastest flow is found at the melt surface.

at the solid-liquid interfaces:

$$\nabla\phi\cdot\boldsymbol{n}_{k,v} = (\boldsymbol{n}_{k,v}\times(-\omega r\boldsymbol{e}_\varphi))B_0\boldsymbol{e}_x = \frac{-B_0\omega r\cos(\varphi)r'_{k,v}(z)}{(1 + r'_{k,v}(z)^2)^{1/2}}$$

where $\boldsymbol{n}_{k,v}$ is the vector normal to the solid–liquid interface; the index k stands for the growth interface, v for the melting interface, $r_{k,v}(z)$ the corresponding interface curvature of the growing and melting interface, $u_{t1,t2}$ the tangential component of velocity; $t1$ and $t2$ are two orthogonal local tangential vectors on the surface.

The velocity field and the temperature distribution for the case of the thermocapillary dominated flow (RMF off) are given in Fig. 8a and for the interaction of thermocapillary convection and rotating field in Fig. 8b. The simulation was performed for a Marangoni number $\text{Ma} = 3000$ (equivalent to a zone height of 12 mm and a temperature difference along the free surface of approximately 20°C) which are realistic values for the performed experiments. The aspect ratio was 1.5. The structure of the flow without field is fully three-dimensional (3D), one large, diagonal roll is formed together with some smaller ones in the corners. The break of

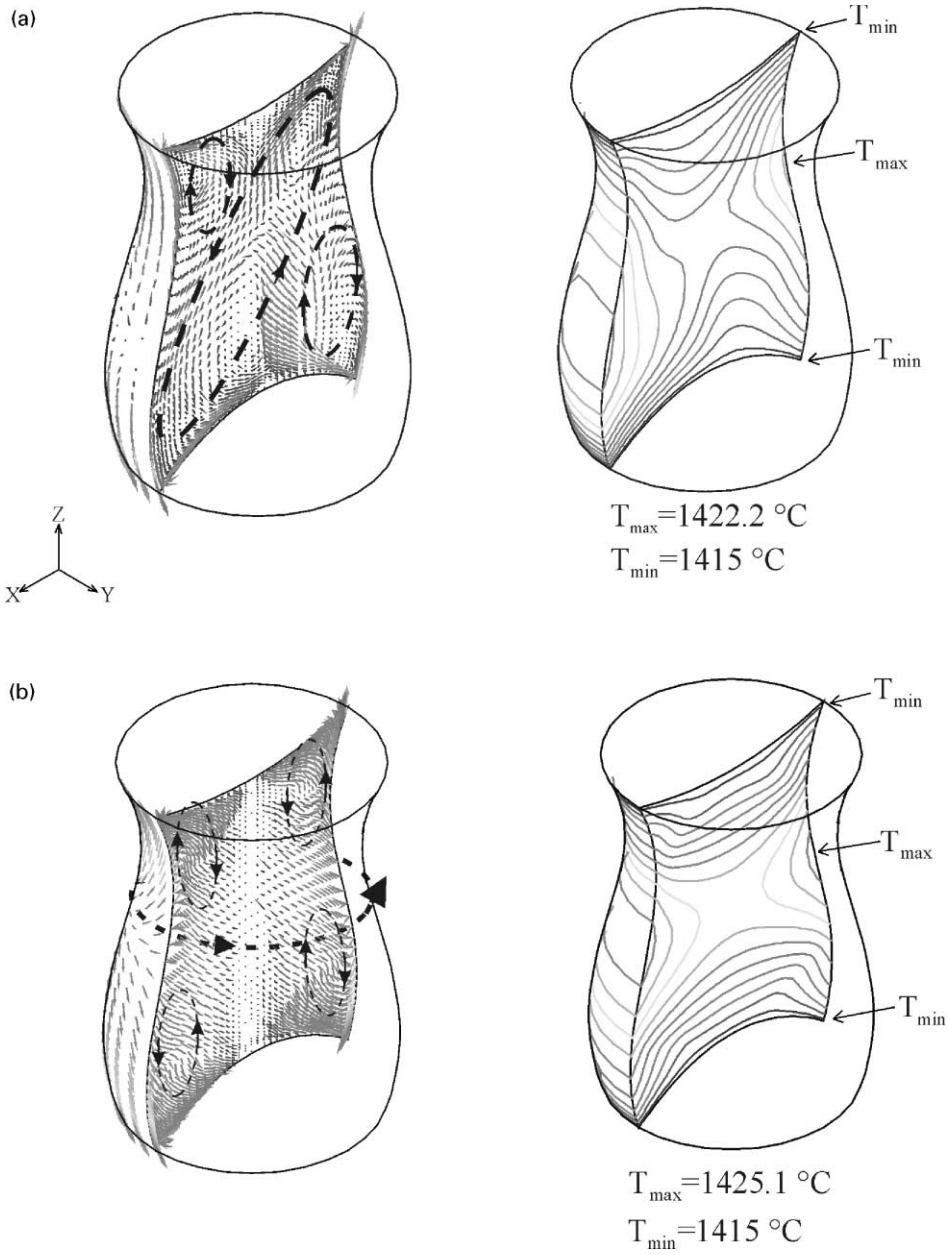

Fig. 8. 3D numerical simulation of a silicon floating zone with aspect ratio = 1.5. Without magnetic field, the 3D, time-dependent flow structure with strong axial and radial components leads to asymmetric isotherms. Applying a RMF, the flow field and the isotherms become axisymmetric, the main flow components point now into the azimuthal direction.

symmetry is reflected in non-symmetric isotherms. The rolls are pulsating and the heat transport is time-dependent with temperature fluctuations $\Delta T \leqslant \pm 0.35^{\circ}\mathrm{C}$. The maximum flow velocity amounts to 15.3 cm/s, pointing in axial/radial direction. Performing the simulation again for $\mathrm{Ma} = 3000$ but now with an applied RMF of $\mathrm{Ta} = 7.8 \times 10^4$, the flow structure

changes drastically.[3] The radial and axial flow components are considerably reduced, now forming nearly axisymmetric tori, in favour of a high azimuthal flow with maximum velocities of $u_\varphi = 14\,\mathrm{cm/s}$. The isotherms become axisymmetric, the fluctuation amplitude is reduced to $\Delta T = \pm 0.02^\circ\mathrm{C}$.

4. Discussion

Several differences are noteworthy when comparing RMF-grown crystals with crystals processed in static magnetic fields:

- No coring or faceting has been observed in any of the RMF grown crystals as it was reported for static magnetic field growth [3,27]. In contrast, the rotating magnetic field actually improves the radial segregation profile.
- We did not find any evidences for TEMC as it may occur by the interaction of static magnetic fields with thermoelectric currents [4]. The generation of TEMC needs a magnetic field perpendicular to concentration differences along isotherms or temperature differences along isoconcentration lines. The RMF changes its direction as a function of time, therefore the requirements for TEMC are not given.
- A significant difference is found in the magnetic induction necessary to improve the dopant distribution: for similar growth parameters, a static magnetic field of approximately 200–250 mT was needed to eliminate microscopic dopant non-uniformities [3], a magnetic induction more than one order of magnitude higher than what is needed in the case of rotating fields. A fact which also results in a much lower power consumptions for the latter case.

Generally speaking, we see a relaminarization of the flow regime due to an increase of the pressure as a consequence of the high azimuthal forced flow. Taylor-vortex type flow instabilities can be generated when employing rotating magnetic fields, provided that the induced flow velocities exceed a certain threshold value [9,23]. However, the appearance of Taylor vortices requires a rigid container wall with no-slip conditions, thus floating zone growth is not affected by this type of flow instabilities.

The origin of the remaining dopant striations in the RMF-dominated flow regime cannot be addressed unambiguously, but several sources might be responsible:

- Time-dependent thermocapillary convection is still interfering with the (axisymmetric) forced azimuthal convection, resulting in a weak remaining time-dependent flow component.
- The forced convection is not exactly axisymmetric, but "wobbles" somewhat. This is a fact which cannot be excluded completely because a slight misalignment of the sample with respect to the center of the magnet or a certain deviation of one coil compared to the other ones is rather likely but difficult to prove with standard Hall probes because of the low induction of the field.
- The forced flow becomes unstable because of the high flow velocities generated by the RMF (compare Fig. 3). For a melt diameter of 14 mm and a flow velocity of 11 cm/s as it was derived from the frequency analysis, a Reynolds number $\mathrm{Re} = 2200$ is calculated ($\mathrm{Re} = vl/v$ with v: flow velocity, l: characteristic length, i.e. melt radius, and v: kinematic viscosity). In general, the transition from laminar to time-dependent or even turbulent flow is in the range of $\mathrm{Re} \approx 10^3$, but it also depends strongly on the configuration and the boundary conditions.

Which one of these factors plays the most important role, cannot be separated and an interaction of all of them is actually quite likely.

Due to the relatively low rotation frequencies of the RMF, no interference was observed between the RMF and the zone shape in any of the experiments. Neither a pinching effect like in the RF-heated needle eye technique was detectable nor an influence of Joule heating as it has been reported for the stirring of large volume mercury melts [28]. For the investigated parameter range, the influence of the magnetic field on the interface

[3] A Taylor number $\mathrm{Ta} = 7.8 \times 10^4$ corresponds to a magnetic induction of 21 mT for the case of $r = 4$ mm or an induction of 6.9 mT and a radius of 7 mm, respectively.

curvature was rather weak compared to the results reported for Bridgman or THM growth [13,29] where a flattening or even a change from a concave to a convex growth front was observed. The secondary (poloidal) flow, which is responsible for the significantly altered heat and mass transport in the latter growth arrangements with rigid cylindrical walls, is considerably lower in the FZ-case due to the release of the pressure imbalance (compare e.g. [30]) over the free surface.

5. Summary

Silicon floating zone experiments have been performed using rotating magnetic fields of $0 \leqslant B \leqslant 7.5\,\mathrm{mT}/50\,\mathrm{Hz}$. Phosphorus, arsenic, and antimony have been used as dopants, crystal diameters were in the range of 8–14 mm. Thermocapillary driven convection was controlled to a large extent by the rotating fields. The main results are:

- *Microsegregation*: The intensity of the dopant non-uniformities is strongly reduced by RMF's of only a few millitesla. Their frequency distribution is shifted to higher values (e.g. from approximately 0.1–2 Hz for $B = 0\,\mathrm{mT}$ to $\approx 2.7 \pm 0.2\,\mathrm{Hz}$ for the case of $d = 14\,\mathrm{mm}$, $B = 7.5\,\mathrm{mT}/50\,\mathrm{Hz}$, equivalent to a Taylor number of $\mathrm{Ta} = 8.5 \times 10^4$). A relatively sharp transition point can be determined. Below this threshold value, the striation characteristics are defined by thermocapillary convection, above it, the distribution is periodic and typical for RMF-induced forced convection. The threshold value is a function of the melt diameter and lower field strengths are needed for larger melt volumes.
- *Radial segregation*: The fluctuations of the dopant concentration are reduced under the influence of the RMF. The profiles become more symmetric due to the azimuthal forced flow.
- *Axial macrosegregation*: The initial transient becomes steeper in the case of the rotating magnetic field grown parts, indicating a reduced axial and radial mass transport. This can be attributed to the reduction of radial and axial flow components upon application of the field.
- *Interface shape*: If the growth front is asymmetric without field, e.g. due to thermal asymmetries of the furnace, a symmetrization is observed upon application of the field. The curvature is slightly flatter in the RMF grown parts but the effect is not significant.

3D-numerical simulations confirm the change in the flow structure and demonstrate the transition from an irregular, time-dependent regime without field to a quasi-two-dimensional (2D), axisymmetric one under the influence of the RMF:

- The RMF induces a flow with a high azimuthal flow component, which suppresses the axial and radial flow due to thermocapillary convection.
- The generated flow is quasi-2D. Asymmetric isotherms are transformed to more symmetric ones.
- For a non-dimensional Taylor number of $\mathrm{Ta} = 7.8 \times 10^4$ (aspect ratio 1.5), a maximum flow velocity of $v = 14\,\mathrm{cm/s}$ was calculated. This is in good agreement with the flow velocity of 11 cm/s derived experimentally by frequency analysis for $\mathrm{Ta} = 8.5 \times 10^4$ (aspect ratio = 1).
- The maximum flow velocity is induced at the free melt surface; the maximum flow velocity is more than 5 times higher for the case of free surfaces compared to rigid walls.

Acknowledgements

We are indebted to L. Rees-Isele for ampoule preparation and to W. Drayer and St. Rothenbacher for building and maintaining mechanical and control systems.

The work would not have been possible without the financial support granted by the German Federal Minister of Education and Research (BMBF) through DLR under contract numbers 50WM9505 and 50WM9503.

References

[1] A. Cröll, W. Müller-Sebert, K.W. Benz, R. Nitsche, Microgravity Sci. Technol. III/4 (1991) 204.
[2] T. Kaiser, K.W. Benz, J. Crystal Growth 183 (1998) 564.

[3] P. Dold, A. Cröll, K.W. Benz, J. Crystal Growth 183 (1998) 545.
[4] A. Cröll, F.R. Szofran, P. Dold, K.W. Benz, S.L. Lehoczky, J. Crystal Growth 183 (1998) 554.
[5] J.P. Birat, J. Choné, Ironmaking Steelmaking 10 (6) (1983) 269.
[6] K.-H. Spitzer, K. Schwerdtfeger, Trans. Iron Steel Soc. (ISS), I&SM 9 (1990) 57.
[7] E. Dahlberg, AB Atomenergi, Sweden AE-447, 1972.
[8] P.A. Davidson, Mater. Sci. Technol. 1 (1985) 994.
[9] T. Kaiser, K.W. Benz, Phys. Fluids 10 (5) (1998) 1104.
[10] B. Fischer, J. Friedrich, U. Hilburger, G. Müller, Proceedings of the Third International Symposium on Electromagnetic Processing of Materials, EPM2000, Nagoya, Japan, 2000, pp. 497–502.
[11] Y.M. Gel'fgat, Proceedings of the IAF-conference, IAF-94-J.4.251, Jerusalem, Israel, 1994.
[12] M. Salk, M. Fiederle, K.W. Benz, A.S. Senchenkov, A.V. Egorov, D.G. Matioukhin, J. Crystal Growth 138 (1994) 161.
[13] A.S. Senchenkov, I.V. Barmin, A.S. Tomson, V.V. Krapukhin, J. Crystal Growth 197 (1999) 552.
[14] K. Hoshikawa, H. Kohda, H. Hirata, H. Nakanishi, Japan J. Appl. Phys. 19 (1) (1980) L33.
[15] K. Yamashita, S. Kobayashi, T. Aoki, Y. Kawata, T. Shiraiwa, Semicond. Fabrication: Technol. Metrol. ASTM STP 990 (1989) 7.
[16] P. Dold, K.W. Benz, Cryst. Res. Technol. 32 (1) (1997) 51.
[17] A. Cröll, P. Dold, T. Kaiser, F.R. Szofran, K.W. Benz, J. Electrochem. Soc. 146 (6) (1999) 2270.
[18] B. Fischer, J. Friedrich, H. Weimann, G. Müller, J. Crystal Growth 198/199 (1999) 170.
[19] P. Dold, K.W. Benz, Progr. Cryst. Growth Characterization Mater. 38 (1–4) (1999) 7.
[20] B. Fischer, J. Friedrich, C. Kupfer, G. Müller, D. Vizman, Proceedings of the Third International Conference on Transfer Phenomena in MagnetoHydroDynamic and Electroconducting Flows, Aussois, France, 1997, pp. 337–342.
[21] Y.M. Gel'fgat, J. Priede, M.Z. Sorkin, Proceedings of the International Conference on Energy Transfer in MHD Flows, Cadarache, France, 1992, pp. 181–186.
[22] A. Senchenkov, I. Friazinov, M. Zabelina, Proceedings of the First International Symposium on Hydromechanics and Heat/Mass Transfer in Microgravity, Perm/Moscow, 1991, pp. 455–459.
[23] P. Marty, L.M. Witkowski, P. Trombetta, T. Tomasino, J.P. Garandet, in: A. Alemany, P. Marty, J.P. Thibault (Eds.), Transfer Phenomena in Magnetohydrodynamic and Electroconducting Flows, Vol. 51, Fluid Mechanics and its Applications, Kluwer Academic Publishers, Dordrecht, 1998, pp. 327–343.
[24] M. Witkowski, J.S. Walker, Proceedings of the PAMIR Conference, 2000.
[25] M.S. Engelman, FIDAP 7.6, Fluid Dynamics Inc., Evanston, IL, 1998.
[26] T. Kaiser, Ph.D. Thesis, Kristallographisches Institut, University of Freiburg, 1998.
[27] M. Kimura, H. Arai, T. Mori, H. Yamagishi, J. Crystal Growth 128 (1993) 282.
[28] T. Robinson, K. Larsson, J. Fluid Mech. 60 (4) (1973) 641.
[29] J. Friedrich, C. Kupfer, B. Fischer, G. Müller, Proceedings of the Third International Conference on Transfer Phenomena in MagnetoHydroDynamic and Electroconducting Flows, Aussois, France, 1997, pp. 439–444.
[30] P.A. Davidson, F. Boysan, Appl. Sci. Res. 44 (1987) 241.
[31] V.M. Glazov, S.N. Chizhevskaya, N.N. Glagoleva, Liquid Semiconductors, Plenum Press, New York, 1969.
[32] M. Schulz, H. Weiss, Technology of Si, Ge, and Sic, Landolt-Börnstein, Vol. 17c, Springer, Berlin, 1984.
[33] H. Kölker, J. Crystal Growth 50 (1980) 852.
[34] S.C. Hardy, J. Crystal Growth 69 (1984) 456.